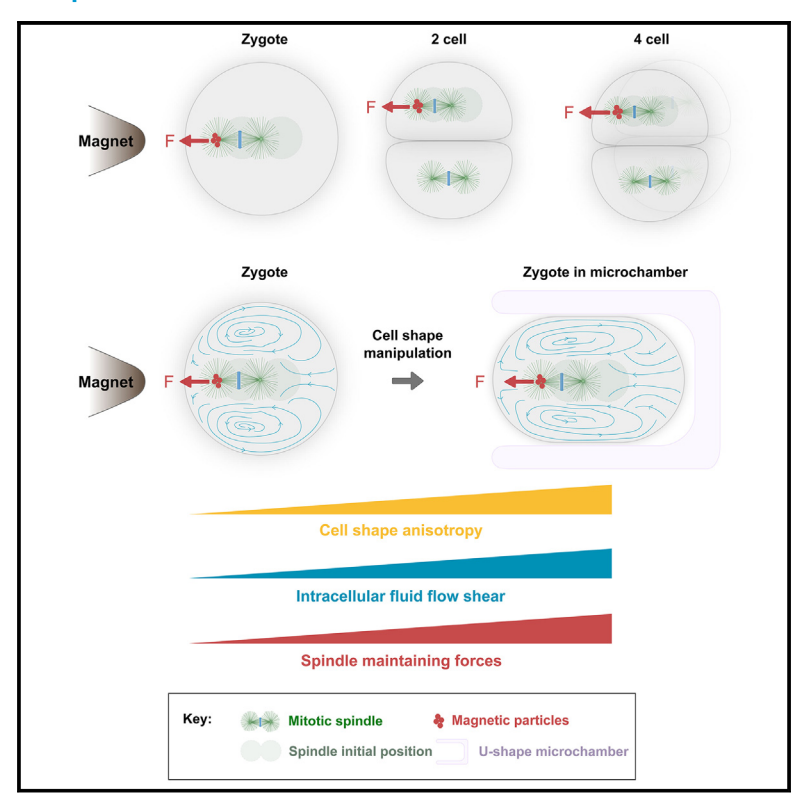
## **Current Biology**

## Cell shape modulates mitotic spindle positioning forces via intracellular hydrodynamics

#### **Graphical abstract**



#### **Authors**

Jing Xie, Javad Najafi, Aude Nommick, ..., Benjamin Lacroix, Julien Dumont, Nicolas Minc

#### Correspondence

nicolas.minc@ijm.fr

#### In brief

Using *in vivo* magnetic tweezers to measure forces needed to move mitotic spindles in early-developing sea urchin embryos, Xie et al. uncover a hydrodynamic mechanism for how cell geometry impacts the mechanics of spindle positioning. Their result suggests that cell shape anisotropy can dampen cytoplasm flows and spindle mobility.

#### **Highlights**

- Spindle positioning forces are measured with magnetic tweezers in early embryos
- These forces increase during early development
- The elongated cell shape of blastomeres accounts for this mechanical enhancement
- Cell shape anisotropies dampen cytoplasm flows and consequent spindle mobility

## **Current Biology**



#### Report

# Cell shape modulates mitotic spindle positioning forces via intracellular hydrodynamics

Jing Xie, 1,2,3,4,5 Javad Najafi, 1,2 Aude Nommick, 1,2 Luc Lederer, 1,2 Jeremy Salle, 1,2 Serge Dmitrieff, 1,2 Benjamin Lacroix, 1,6 Julien Dumont, 1 and Nicolas Minc 1,2,7,8,\*

<sup>1</sup>Université Paris Cité, CNRS, Institut Jacques Monod, 75013 Paris, France

<sup>2</sup>Equipe Labellisée LIGUE Contre le Cancer, 75013 Paris, France

<sup>3</sup>Present address: Institut Curie, PSL Research University, CNRS UMR144, Laboratoire Biologie Cellulaire et Cancer, 75005 Paris, France <sup>4</sup>Present address: Institut Curie, PSL Research University, Sorbonne Université, CNRS UMR3664, Laboratoire Dynamique du Noyau, 75005

<sup>5</sup>Present address: Institut Curie, PSL Research University, Sorbonne Université, CNRS UMR168, Laboratoire Physique des Cellules et Cancer, 75005 Paris, France

<sup>6</sup>Present address: Université de Montpellier, Centre de Recherche en Biologie cellulaire de Montpellier (CRBM), CNRS UMR 5237, 1919 Route de Mende, 34293 Montpellier Cedex 5, France

<sup>7</sup>X (formerly Twitter): @MincLab

<sup>8</sup>Lead contact

\*Correspondence: nicolas.minc@ijm.fr https://doi.org/10.1016/j.cub.2024.11.055

#### **SUMMARY**

The regulation of mitotic spindle positioning and orientation is central to the morphogenesis of developing embryos and tissues. <sup>1–5</sup> In many multicellular contexts, cell geometry has been shown to have a major influence on spindle positioning, with spindles that commonly align along the longest cell shape axis. <sup>6–14</sup> To date, however, we still lack an understanding of how the nature and amplitude of intracellular forces that position, orient, or hold mitotic spindles depend on cell geometry. Here, we used *in vivo* magnetic tweezers to directly measure the forces that maintain the mitotic spindle in the center of sea urchin cells that adopt different shapes during early embryo development. We found that spindles are held by viscoelastic forces that progressively increase in amplitude as cells become more elongated during early development. By coupling direct cell shape manipulations in microfabricated chambers with *in vivo* force measurements, we establish how spindle-associated forces increase in dose dependence with cell shape anisotropy. Cytoplasm flow analysis and hydrodynamic simulations suggest that this geometry-dependent mechanical enhancement results from a stronger hydrodynamic coupling between the spindle and cell boundaries, which dampens cytoplasm flows and spindle mobility as cells become more elongated. These findings establish how cell shape affects spindle-associated forces and suggest a novel mechanism for shape sensing and division positioning mediated by intracellular hydrodynamics with functional implications for early embryo morphogenesis.

#### **RESULTS AND DISCUSSION**

## Mitotic spindles are held by viscoelastic forces in the center of early blastomeres

During the early development of sea urchin embryos, as in many invertebrate and vertebrate embryos, zygotes and blastomeres divide symmetrically, by positioning mitotic spindles in the cell center. <sup>15–18</sup> As a result of cell-cell adhesion and confinement by embryo enveloping layers, divided blastomeres also change shape and become more anisotropic, transitioning from a round zygote to two hemispherical 2-cell blastomeres and four ellipsoidal 4-cell blastomeres <sup>16,19</sup> (Figures 1A and 1B). We first sought to exploit these shape variations to test how spindle positioning forces may depend on cell geometry. To measure forces that hold spindles in the center of early blastomeres, we applied calibrated forces on mitotic spindles along the spindle axis in zygotes and 2- and 4-cell blastomeres, using *in vivo* magnetic tweezers (Figures 1C–1H; Video S1). These assays rely on the

injection of specific magnetic beads that recruit dynein to self-target themselves to centrosomes and form compact aggregates that stay attached to centrosomes throughout early embryo development. These beads also form aggregates in vitro, which allows for the calibration of the magnetic force as a function of aggregate size and distance to the magnet tip, by tracking beads or aggregate velocities in test viscous fluids. 21

Upon magnetic force application on one spindle pole, spindles at all stages moved as compact objects, allowing us to record displacement-time behavior. Interestingly, these displacement-time curves exhibited similar signatures from the 1-cell stage to the 4-cell stage. First, the spindle moved at constant speed following a linear viscous regime, and then it slowed down reflecting elastic forces that limit spindle displacements. On longer timescales, the spindle recovered a constant speed, suggesting a progressive fluidization of elastic elements (Figure 1I). In agreement with the existence of an elastic response, when the force was released, spindles recoiled back toward their initial position



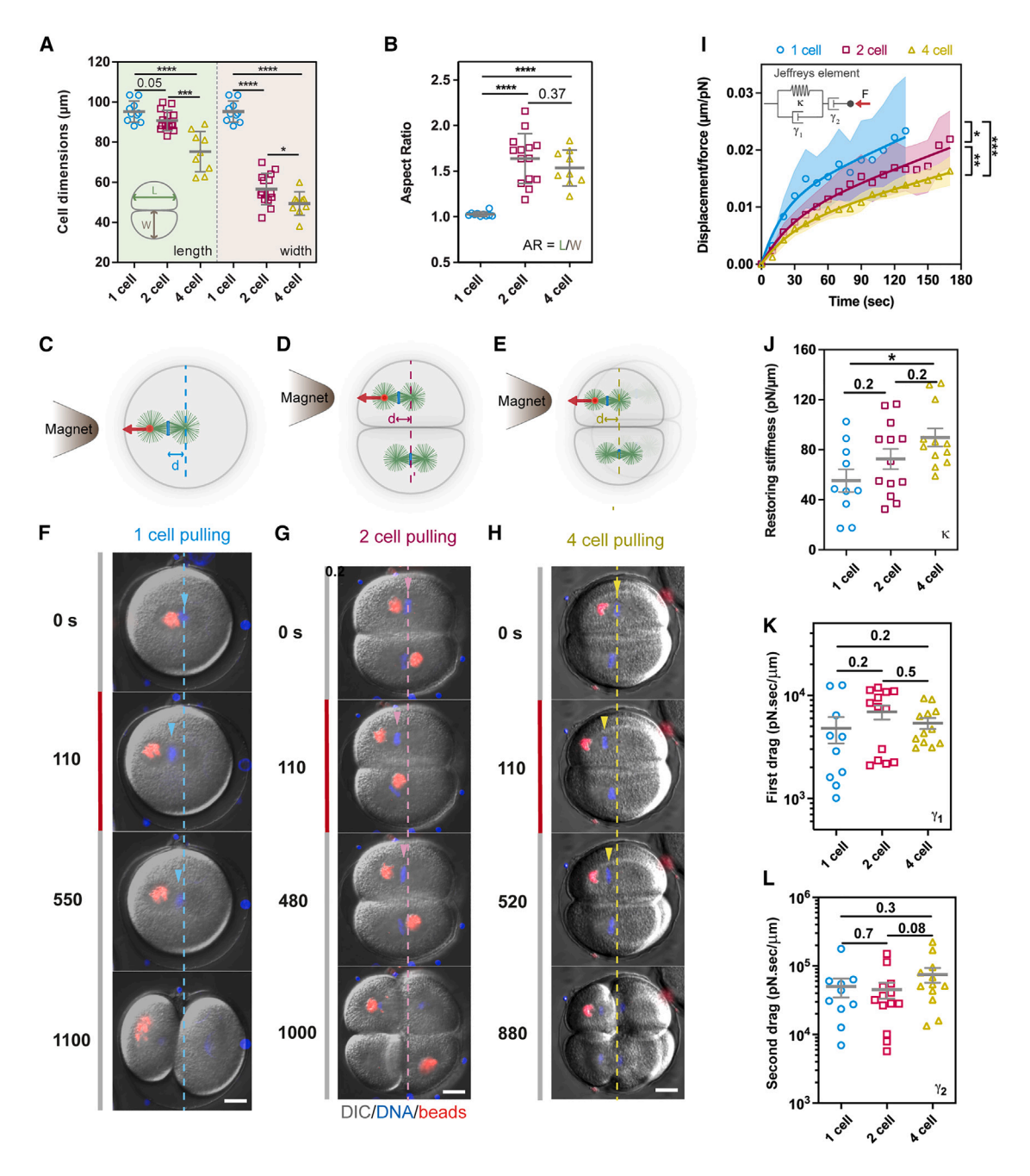


Figure 1. Mitotic spindles are held in the cell center by viscoelastic forces that increase with developmental stages

(A and B) Quantification of cell length, width, and aspect ratio of 1-, 2-, and 4-cell-stage blastomeres (n = 10, 14, and 9, respectively).

(C–H) Schemes and time lapses of metaphase spindles at 1-cell stage (C and F), 2-cell stage (D and G), and 4-cell stage (E and H), displaced by magnetic forces applied parallel to the spindle axis, and recoiling upon force cessation. Dotted lines correspond to the initial centered position of the spindle, and arrowheads indicate the position of chromosomes.

- (J) Spindle restoring stiffness for the same cells and conditions as in (I), computed using fits to the Jeffreys' model.
- (K) Spindle short-term drag coefficient for the same cells and conditions as in (I), computed using fits to the Jeffreys' model.
- (L) Spindle long-term drag coefficient for the same cells and conditions as in (I), computed using fits to the Jeffreys' model.

Error bars correspond to  $\pm$ SEM. Results in (I) were compared using a Kolmogorov-Smirnov test and those in (A), (B), (J), (K), and (L) using a two-tailed Mann-Whitney test. T test p values are reported on the graph or indicated as \*p < 0.05, \*\*p < 0.01, \*\*\*\*p < 0.001, \*\*\*\*p < 0.0001. Scale bars, 20  $\mu$ m. See also Figure S1 and Video S1.

<sup>(</sup>I) Time evolution of spindle displacement normalized by the applied magnetic force for metaphase spindles in 1-cell, 2-cell, and 4-cell embryos (n = 10, 13, and 12 cells, respectively). The bold lines correspond to fits of the data using a Jeffreys' viscoelastic model. Error bars represented as shades in these curves correspond to  $\pm$ SD/2.



at the cell center. However, this recovery was only partial, with spindles recoiling only  $\sim\!50\%$  of the distance moved under force, indicating a significant dissipation of stored elastic energy (Figures S1A and S1B). We conclude that mitotic spindles from the 1-cell stage to the 4-cell stage are held in the cell center by viscoelastic spring-like forces.

To compute the magnitude of these forces, we fitted rising and relaxation responses with a 3-element Jeffreys' viscoelastic model<sup>22-24</sup> (Figure 1I). This allowed us to extract a spindle restoring stiffness, κ, that quantifies the amplitude of elastic forces normalized by the distance the spindle moved from the cell center, as well as to extract spindle short-time and longtime viscous drags,  $\gamma_1$  and  $\gamma_2$ , defining two viscoelastic timescales  $\tau_1 = \gamma_1/\kappa$  and  $\tau_2 = \gamma_2/\kappa$ . Remarkably, these analyses revealed that spindle restoring stiffness increased gradually during early development, from values of  $55.34 \pm 28.8 \text{ pN/}\mu\text{m}$  ( $\pm\text{SD}$ ) for zygotes to  $72.65 \pm 29.06$  pN/ $\mu$ m for 2-cell-stage blastomeres and 89.76 ± 25.08 pN/μm for 4-cell-stage blastomeres (Figure 1J). This shows that displacing the spindle 5 μm away from the cell center (few % of cell length) requires large forces that increase from  $\sim$ 276 to  $\sim$ 363 and  $\sim$ 449 pN, from the 1-cell to the 2-cell and 4-cell stages, respectively. Viscous drags were more variable, but they also tended to increase at later stages, with viscoelastic timescales that remained at similar values of  $\tau_1 \sim 1$  min and  $\tau_2 \sim 15$  min independent of developmental stages, in agreement with spindle recoils occurring at the same rates (Figures S1B-S1D). These results indicate a progressive rise in the forces that hold spindles in the cell center when cells become smaller and more elongated during early development.

## Cell shape anisotropy may enhance cytoplasm viscoelastic resistance on spindles

Viscoelastic forces holding spindles in the cell center were previously reported and attributed either to networks of microtubules (MTs) that reach to the cell cortex to push with length-dependent forces<sup>25,26</sup> or alternatively to the mere gellike viscoelastic properties of bulk cytoplasm that baths the spindle.<sup>22,27</sup> A central difference between these two models resides in the presence (respectively, absence) of numerous MTs that reach to the cell surface.<sup>27</sup> Therefore, to distinguish between these two models, we performed immunostaining to label MTs, F-actin, and DNA and used Airyscan high-resolution confocal microscopy to measure the distance between MT + TIPs and the actin-rich cortex in metaphase from the 1-cell stage to the 16-cell stage (Figures 2A, S1E, and S1F). The mean distance was 14.48  $\pm$  2.65  $\mu$ m ( $\pm$ SD) in zygotes, and it gradually reduced at subsequent stages to reach a distance of only  $2.54 \pm 2.34 \mu m$ at the 16-cell stage (Figures 2B and S1G-S1J). These distances represented a relatively stable fraction of  $\sim 15\%$  of cell length from the 1-cell stage to the 4-cell stage but sharply decreased to only  $\sim$ 6% of cell length from the 8-cell stage onward. In addition, the number of MTs reaching a distance less than 2 µm of the actin-rich cortex was 0, 0.4 and 3.5 MTs/cell at the 1-, 2-, and 4-cell stages but increased to 17.9 and 24.3 MTs/cell at the 8and 16-cell stages (Figures 2C, S1G, and S1H). These analyses suggest that spindles are mostly uncoupled from the cell surface up to the 4-cell stage in these embryos, favoring a primary role for cytoplasm viscoelasticity in holding spindles in the center of early blastomeres.

To understand if and how viscoelastic restoring forces associated to cytoplasm material properties could increase in amplitude as cells become smaller and more elongated, we implemented finite-element hydrodynamic simulations.<sup>24,28</sup> Given that the spindle is enclosed in a dense network of endoplasmic reticulum,<sup>22</sup> with near ellipsoidal shape, we modeled it as a rigid impermeable ellipsoidal object with dimensions taken from experimental measurements at different developmental stages (Figures S1K and S1L). Cell shapes and sizes were obtained by cutting the 1-cell sphere into two hemispheres for the 2-cell stage and into four quarters for the 4-cell stage (Figure 2D; Table S1). The cytoplasm was implemented as a viscoelastic fluid behaving as in the Jeffreys' model used to analyze experimental curves and obeying no-slip conditions at the interface with both spindle and cell boundaries.<sup>24</sup> To simulate magnetic pulls on spindles, a constant step force was applied to one half of the spindle, using a boundary load. We simulated both pulling and relaxation and fitted the displacement-time curve of the spindle, as in experiments, to compute simulated values of restoring stiffnesses and viscous drags. Finally, these simulations also allowed us to predict cytoplasm flow fields and amplitudes, which accompany spindle movements in the cell interior.

To isolate the sole effect of cell size, we first ran simulations in spheres of reducing volumes and scaled spindle size according to experimental measurements, but we kept other parameters identical (Figure 2F; Table S1). These simulations did not predict any increase in restoring stiffnesses or drags, as observed in experiments, presumably because spindle size scale with cell size during early sea urchin embryogenesis. <sup>29</sup> Next, we simulated the effect of both cell shape and size variations, as in experiments (Figure 2E; Video S2). Remarkably, these simulations predicted that an increase in cell shape anisotropy, as observed in early blastomeres, can lead to a progressive increase in both spindle restoring stiffnesses and drags, in close agreement with experimental behavior (Figures 2F and S1M). These simulation results suggest that an anisotropic cell shape may be sufficient to enhance cytoplasm mechanical resistance on mitotic spindles.

## Manipulation of cell shape alters cytoplasm viscoelastic resistance on spindles

To experimentally test the impact of cell shape on spindle positioning forces in experiments, we first applied forces orthogonal to the spindle axis and compared the response between round isotropic zygotes and elongated 2-cell-stage blastomeres. In both cells, this mode of force exertion caused spindles to translate as well as rotate to reorient toward the magnet tip (Figures 3A-3D; Video S3). Strikingly, translating restoring stiffness and drag were both significantly increased by 168.8% and 166.1%, respectively, between zygotes and 2-cell-stage blastomeres. Simulations reproduced this increase, yielding relative values matching experimental measurements (Figures 3E-3H and S2A-S2D). In addition, when the force was released, in both simulations and experiments, the spindle rotated back, restoring rotationally stored elastic energy. This demonstrates that the cytoplasm can also apply restoring torques on spindles, to spring them back along their initial axis (Video S4). Therefore, spindle maintaining forces both along and orthogonal to the spindle axis become stronger with cell shape anisotropies.



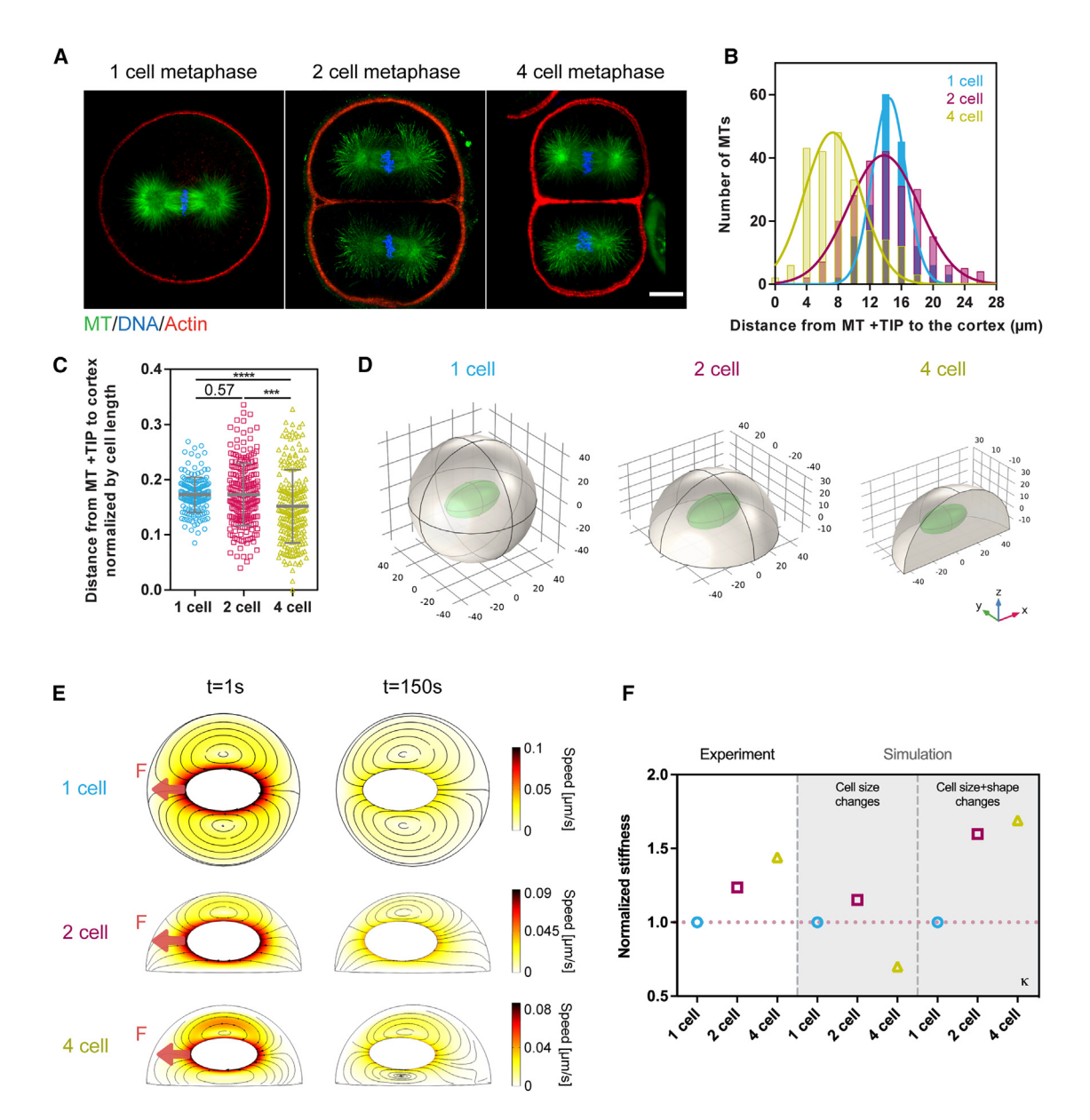


Figure 2. Changes in spindle restoring stiffness with cell shape may rely on cytoplasm viscoelasticity and changes in hydrodynamic boundary conditions

- (A) Airyscan confocal images of sea urchin embryos at 1-cell (left), 2-cell (middle), and 4-cell stage (right) in metaphase fixed and stained for microtubules (MTs), DNA, and F-actin.
- (B) Distance from MT + TIPs to the actin cortex in 1-cell, 2-cell, and 4-cell stage embryos at metaphase (n = 168, 229, and 220 MTs from 4 independent embryos, respectively).
- (C) Distance from MT + TIPs to the actin cortex normalized by cell length for the same conditions as in (B).
- (D) Schematic of cell and spindle geometries used to simulate the response of spindles to applied forces in a viscoelastic cytoplasm.
- (E) Stream lines and fluid flow speeds corresponding to two time points (beginning and end of pulling) of hydrodynamic simulations of spindles moving under force in a viscoelastic medium confined by cell boundaries at different developmental stages.
- (F) Restoring stiffness normalized by the 1-cell-stage value compared between data from experiments and different sets of simulation, considering changes in cell size only or in both cell size and shape. The red dotted line corresponds to a value of 1.

Results were compared using a two-tailed Mann-Whitney test. p values are reported on the graph or indicated as \*\*\*p < 0.001, \*\*\*\*p < 0.0001. Scale bars, 20 µm. See also Figure S1, Video S2, and Table S1.

To more directly test the contribution of cell shape anisotropy to the amplitude of forces that hold spindles, independently of developmental stages, we next compared parallel and orthogonal pulls in 2-cell-stage elongated blastomeres. We found that spindles were significantly harder to displace in orthogonal pulls, with a restoring stiffness and drag that increased by 154.2% and 157.1%, respectively, when compared with translational pulls. Simulations reproduced this increase in both



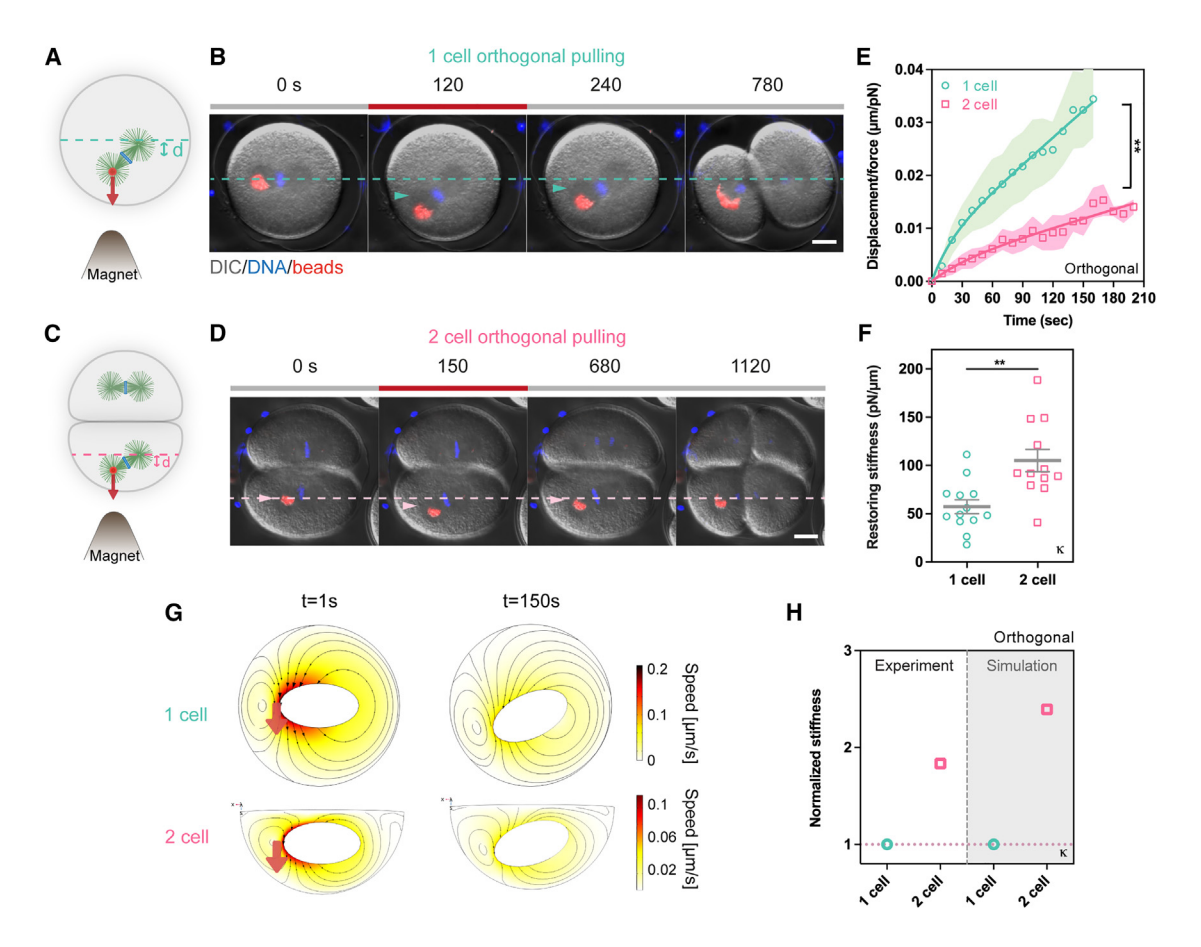


Figure 3. Cell shape anisotropy enhances spindle restoring stiffness in early embryos

(A–D) Schemes and time lapses of metaphase spindles at the 1-cell stage (A and B) and 2-cell stage (C and D), displaced by magnetic forces applied orthogonal to the spindle axis, and recoiling upon force cessation. Dotted lines correspond to the initial position and orientation of the spindle, and arrow heads indicate the position of the pulled spindle pole.

- (E) Time evolution of spindle displacement normalized by the applied force in 1-cell and 2-cell embryos (n = 14 and 10 cells, respectively). The bold lines correspond to fits of the data using a Jeffreys' viscoelastic model. Error bars represented as shades in these curves correspond to  $\pm$ SD/2.
- (F) Orthogonal spindle restoring stiffness for the same cells and conditions as in (E), computed using fits to the Jeffreys' model (n = 13 and 11 cells, respectively). Error bars correspond to ±SEM.
- (G) Stream lines and fluid flow speeds corresponding to two time points (beginning and end of pulling) of hydrodynamic simulations of spindles moving under a force orthogonal to the spindle axis in a viscoelastic medium confined by cell boundaries in rounded zygotes vs. elongated 2-cell blastomeres.
- (H) Restoring stiffness normalized by the 1-cell-stage value compared between experiments and simulations. The red dotted line corresponds to a value of 1. Results in (E) were compared using a Kolmogorov-Smirnov test and those in (F) using a two-tailed Mann-Whitney test. T test *p* values are reported as \*\**p* < 0.01. Scale bars, 20 μm.

See also Figure S2, Video S3, and Table S1.

stiffness and drags, yielding relative values matching experimental measurements, suggesting that cell shape hydrodynamic confinement effect may be more pronounced when moving spindles along the shortest dimension of the cell (Figures S2G–S2K).

Next, we experimentally rounded 2-cell-stage blastomeres using a transient treatment with calcium-free sea water, which disrupts cell-cell adhesion. This caused initially elongated blastomeres to become round within a few minutes, without affecting cell volume, metaphase duration, or spindle size (Figures S2L–S2O). Using magnetic tweezers, we computed a reduction of both spindle restoring stiffness and viscous drag of 0.83× and 0.67×, respectively, as compared with those of control elongated blastomeres, which matched hydrodynamic simulation predictions (Figures S2Q–S2U). Together, these results

demonstrate how cell geometry may modulate cytoplasm viscoelastic resistance on mitotic spindles.

Finally, we performed the converse experiment, and increased cell shape anisotropy to test impact on spindle positioning forces. Starting with round zygotes, we devised U-shaped microfabricated chambers of various dimensions made in SU-8 resin, which protrude above a coverglass, allowing for cell geometry to be altered while applying magnetic forces with the tweezer system (Figure 4A; Video S4). Eggs were gently pushed into chambers using a glass needle, injected with magnetic beads, and then fertilized (Figures S3A–S3C). To explore dose-dependent effects, we used two sets of chambers in which cells were pushed into elongated shapes of mean aspect ratio of 1.24 and 1.49, respectively (Figures 4A–4E). In chambers,



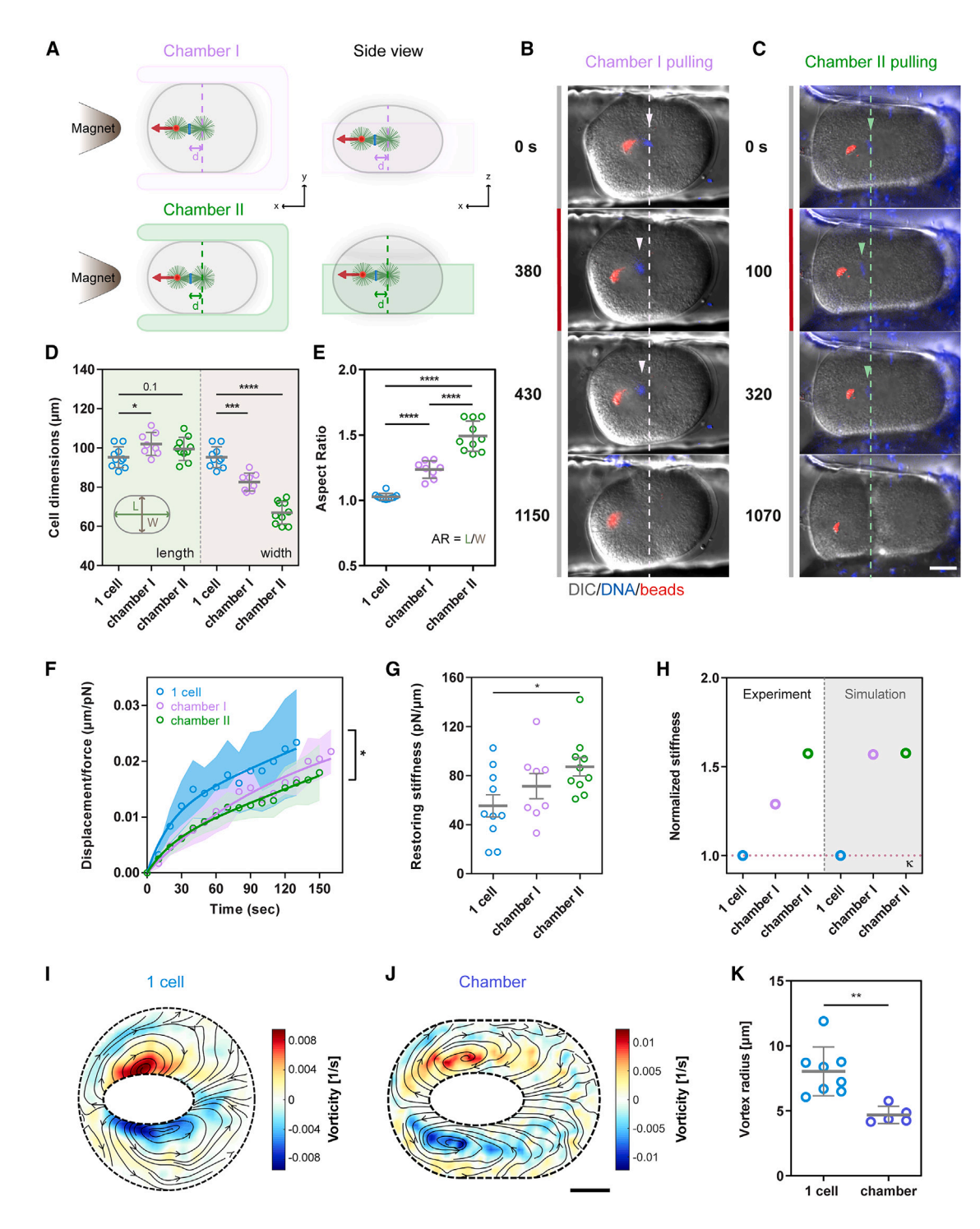


Figure 4. Cell shape anisotropy enhances the viscoelastic resistance of bulk cytoplasm on mitotic spindles

(A) Schemes representing experiments designed to change cell shapes by forcing zygotes into chambers of different geometries.

(B and C) Time lapses of metaphase spindles in cells shaped in chamber I (B) and chamber II (C) with magnetic beads bound to one spindle pole, displaced by magnetic forces applied parallel to the spindle axis from the presence of a magnet tip (red line), and recoiling upon force cessation. Dotted lines correspond to the initial centered position of the spindle, and arrowheads indicate the positions of chromosomes.

- (D and E) Cell size and aspect ratio quantified as indicated in the inset for cells in control and in chambers (n = 10, 8, and 10 cells, respectively).
- (F) Time evolution of the displacement normalized by applied force of metaphase spindles at 1-cell stage in control, in chamber I and in chamber II (n = 10, 8, and 10 cells, respectively). Error bars represented as shades in these curves correspond to  $\pm$ SD/2.
- (G) Restoring stiffness of mitotic spindles for the same cells and conditions as in (F) (n = 10, 8, and 10 cells, respectively). Error bars correspond to ±SEM.
- (H) Restoring stiffness normalized by the 1-cell value in indicated conditions for experimental data vs. simulations.



metaphase spindles moved with external magnetic forces exhibited a displacement that reflected a viscoelastic behavior similar to control and partially relaxed back toward the cell center when the force was removed (Figures 4F and S3E; Video S4). Interestingly, the measured restoring stiffness was significantly higher than in control round zygotes, increasing by 1.29x in the first set of chambers and by 1.57× in the more anisotropic chambers (Figure 4G). Viscous drags were also increased by 1.27 x and 1.22 x, respectively (Figure S3D). By performing simulations using the 3D rectangular cuboid shape of eggs pushed into the two sets of chambers, we predicted an increase of restoring stiffness as well as viscous drags similar to experiments in the two sets of chambers (Figures 4H, S3F, and S3G). These results directly support a significant impact of cell shape anisotropy on the amplitude of viscoelastic forces that hold spindles in the cell center.

## Cell shape anisotropy dampens cytoplasm viscoelastic flows around moving spindles

Inspection of cytoplasm viscoelastic flows, generated along moving and recoiling spindles in simulations, revealed the presence of specific flow streams and recirculation, which appeared to be influenced by different boundary conditions in varying cell shapes (Figures 2E and 3G; Video S2). To test if flow amplitudes and arrangements could be impacted by cell shape in experiments, we used particle image velocimetry of large granules in cells to map flows created along spindle pulls in round and shape-manipulated zygotes. 22,24 In both control round zygotes and deformed ones in microchambers, flows exhibited two large vortices on the sides of moving spindles, indicative of large cytoplasm fluid shear in between the cell and spindle boundaries (Figures 4I and 4J). Interestingly, the size of vortices, measured as the width of the gradient in flow velocities, was much smaller in eggs deformed in chambers, as compared with control round eggs, indicating a much higher shear when cell shapes are more anisotropic (Figures 4K and S3H). Accordingly, by simulating fluid flows caused by spindle movements in diverse cell geometries, we predicted a dose-dependent decrease in the size of vortices and thus an increase in fluid shear with cell shape anisotropy, demonstrating how narrower cell cross-section can dampen fluid flows to increase cytoplasm viscoelastic resistance on spindles (Figures S3I-S3L). We conclude that cell shape can impact spindle positioning forces—through a hydrodynamic coupling between the spindle and the cell surfacethat becomes more prominent as cells become more elongated

The forces that position and orient mitotic spindles are fundamental regulators of tissue morphogenesis, but they have only been rarely measured. <sup>22,25,30</sup> Here, using *in vivo* magnetic tweezer to directly measure spindle maintaining forces in intact embryos at multiple developmental stages, we discovered that these forces increase in magnitude with developmental stages,

as a consequence of a progressive increase in blastomere shape anisotropy. Such increase may have a functional implication for spindle stability during development, by maintaining a relative spindle centering precision mostly constant as cells become smaller<sup>25,26</sup> and also by limiting the impact of large surface stresses associated to acto-myosin contractility inherent to cell division and shape changes on spindle positioning.<sup>28,31-33</sup> Simulations and cytoplasm flow analysis suggest that this shapedependent enhancement emerges from enhanced shear in the cytoplasm, which increases viscoelastic resistance, akin to a piston effect. 24,34,35 Therefore, an important output of this study is to put forward a "cell shape-sensing" mechanism based on the influence of cellular boundaries on cytoplasm hydrodynamics with consequences for the mechanics of organelle positioning. Such mechanisms also suggest that the shape and size of cells will impact the amplitude of cytoplasm streaming flows, which were proposed to influence cytoplasm homogenization or multicellular morphogenesis in various organisms. 31,36-39 Future work addressing in quantitative terms how cytoplasm fluid mechanics intersects with cell geometry will provide important insights into mechanisms of organelle positioning and tissue morphogenesis.

#### **RESOURCE AVAILABILITY**

#### **Lead contact**

Further information and requests for resources and reagents should be directed to and will be fulfilled by the lead contact, Nicolas Minc (nicolas. minc@ijm.fr).

#### **Materials availability**

This study did not generate new unique reagents.

#### **Data and code availability**

- All data needed to evaluate the conclusions in the paper are present in the paper and/or the supplemental information.
- This paper does not report any original code.
- Any additional information required to reanalyze the data reported in this
  work is available from the lead contact upon request.

#### **ACKNOWLEDGMENTS**

We thank all members of the Minc team for the discussion and technical help. J.X. acknowledges the "École Doctorale FIRE—Program Bettencourt," a fellowship from the Chinese Scholarship Council (201708070046), and the Labex "Who Am I." J.N. is supported by a postdoctoral fellowship from the ARC foundation (PDF20191209818) and is an EMBO Non-Stipendiary Fellow (ALTF 881-2019). A.N. is supported by a postdoctoral fellowship from the ARC foundation (PDF2021070004082). We acknowledge the ImagoSeine core facility of the Institut Jacques Monod, a member of Infrastructure en Biologie Santé et Agronomie and France Bio-Imaging infrastructures. This work was supported by the Centre National de la Recherche Scientifique (CNRS) and the Université de Paris; grants from La Ligue Contre le Cancer (EL2021.LNCC/NiM), the Agence Nationale pour la Recherche (ANR, "TiMecaDev"), and the Fondation Bettencourt Schueller ("Coup d'élan"); a scientific subvention from the foundation "Simone and Cino Del

(I and J) Experimental heatmaps of cytoplasm flow streamlines averaged on a duration of 50 s for spindles pulled at the 1-cell stage in spherical control cells (I) and in cells deformed in a chamber (J). Streamlines are superimposed onto a color map of local flow vorticities, ω.

(K) Quantification of flow vortex radius for normal cells and cells deformed in chambers (n = 8 and 5 cells, respectively).

Results in (F) were compared using a Kolmogorov-Smirnov test and those in (D), (E), (G), and (K) using a two-tailed Mann-Whitney test. T test p values are reported on the graph or indicated as \*p < 0.05, \*\*p < 0.01, \*\*\*\*p < 0.001, \*\*\*\*p < 0.0001. Scale bars, 20  $\mu$ m. See also Figure S3, Video S4, and Table S1.



## Current Biology Report

Duca;" and grants from the European Research Council (ERC CoG "Forcaster" no. 647073 and ERC PoC "MagMech" No. 101069173) to N.M.

#### **AUTHOR CONTRIBUTIONS**

Conceptualization, N.M., J.X., and J.N.; methodology, N.M., J.D., B.L., S.D., J.S., A.N., L.L, J.N., and J.X.; writing – original draft, N.M., J.X., and J.N.; writing – review and editing, N.M., J.D., B.L., S.D., J.N., and J.X.

#### **DECLARATION OF INTERESTS**

The authors declare no competing interest.

#### **STAR**\*METHODS

Detailed methods are provided in the online version of this paper and include the following:

- KEY RESOURCES TABLE
- EXPERIMENTAL MODEL AND SUBJECT DETAILS
  - Sea urchin gametes
- METHOD DETAILS
  - Immunostaining
  - o Manipulating cell shape with CaFSW
  - o Fabrication of microchambers
  - Manipulating cell shape with microchambers
  - Magnetic force application
  - Imaging
  - o 3D simulations
- QUANTIFICATION AND STATISTICAL ANALYSIS
  - Magnetic force calibration
  - o Analysis of spindle position
  - o Measuring MT length, dynamics and distance to the cortex
  - Viscoelastic parameter calculation
  - o PIV analysis and shear measurement
  - O Statistical analysis

#### SUPPLEMENTAL INFORMATION

Supplemental information can be found online at https://doi.org/10.1016/j.cub.2024.11.055.

Received: June 26, 2024 Revised: October 21, 2024 Accepted: November 22, 2024 Published: January 3, 2025

#### REFERENCES

- Sallé, J., and Minc, N. (2022). Cell division geometries as central organizers of early embryo development. Semin. Cell Dev. Biol. 130, 3–11. https://doi.org/10.1016/j.semcdb.2021.08.004.
- Godard, B.G., and Heisenberg, C.-P. (2019). Cell division and tissue mechanics. Curr. Opin. Cell Biol. 60, 114–120. https://doi.org/10.1016/j.ceb.2019.05.007.
- Lechler, T., and Mapelli, M. (2021). Spindle positioning and its impact on vertebrate tissue architecture and cell fate. Nat. Rev. Mol. Cell Biol. 22, 691–708. https://doi.org/10.1038/s41580-021-00384-4.
- van Leen, E.V., di Pietro, F., and Bellaïche, Y. (2020). Oriented cell divisions in epithelia: from force generation to force anisotropy by tension, shape and vertices. Curr. Opin. Cell Biol. 62, 9–16. https://doi.org/10.1016/j. ceb.2019.07.013.
- Castanon, I., and González-Gaitán, M. (2011). Oriented cell division in vertebrate embryogenesis. Curr. Opin. Cell Biol. 23, 697–704. https:// doi.org/10.1016/j.ceb.2011.09.009.

- Minc, N., Burgess, D., and Chang, F. (2011). Influence of Cell Geometry on Division-Plane Positioning. Cell 144, 414–426. https://doi.org/10.1016/j. cell.2011.01.016.
- Haupt, A., and Minc, N. (2018). How cells sense their own shape mechanisms to probe cell geometry and their implications in cellular organization and function. J. Cell Sci. 131, jcs214015. https://doi.org/10.1242/ics.214015.
- Théry, M., and Bornens, M. (2006). Cell shape and cell division. Curr. Opin. Cell Biol. 18, 648–657. https://doi.org/10.1016/j.ceb.2006.10.001.
- Hertwig, O. (1893). Ueber den Werth der ersten Furchungszellen fuer die Organbildung des Embryo. Experimentelle Studien am Frosch- und Tritonei. Archiv f. mikrosk. Anat 42, 662–807.
- Bosveld, F., Markova, O., Guirao, B., Martin, C., Wang, Z., Pierre, A., Balakireva, M., Gaugue, I., Ainslie, A., Christophorou, N., et al. (2016). Epithelial tricellular junctions act as interphase cell shape sensors to orient mitosis. Nature 530, 495–498. https://doi.org/10.1038/nature16970.
- Niwayama, R., Moghe, P., Liu, Y.-J., Fabrèges, D., Buchholz, F., Piel, M., and Hiiragi, T. (2019). A Tug-of-War between Cell Shape and Polarity Controls Division Orientation to Ensure Robust Patterning in the Mouse Blastocyst. Dev. Cell 51, 564–574.e6. https://doi.org/10.1016/j.devcel. 2019.10.012.
- Wyatt, T.P.J., Harris, A.R., Lam, M., Cheng, Q., Bellis, J., Dimitracopoulos, A., Kabla, A.J., Charras, G.T., and Baum, B. (2015). Emergence of homeostatic epithelial packing and stress dissipation through divisions oriented along the long cell axis. Proc. Natl. Acad. Sci. USA 112, 5726–5731. https://doi.org/10.1073/pnas.1420585112.
- Campinho, P., Behrndt, M., Ranft, J., Risler, T., Minc, N., and Heisenberg, C.P. (2013). Tension-oriented cell divisions limit anisotropic tissue tension in epithelial spreading during zebrafish epiboly. Nat. Cell Biol. 15, 1405– 1414. https://doi.org/10.1038/ncb2869.
- Scarpa, E., Finet, C., Blanchard, G.B., and Sanson, B. (2018). Actomyosin-Driven Tension at Compartmental Boundaries Orients Cell Division Independently of Cell Geometry In Vivo. Dev. Cell 47, 727–740.e6. https://doi.org/10.1016/j.devcel.2018.10.029.
- Wühr, M., Tan, E.S., Parker, S.K., Detrich, H.W., and Mitchison, T.J. (2010). A model for cleavage plane determination in early amphibian and fish embryos. Curr. Biol. 20, 2040–2045. https://doi.org/10.1016/j.cub. 2010.10.024.
- Pierre, A., Sallé, J., Wühr, M., and Minc, N. (2016). Generic Theoretical Models to Predict Division Patterns of Cleaving Embryos. Dev. Cell 39, 667–682. https://doi.org/10.1016/j.devcel.2016.11.018.
- Zernicka-Goetz, M. (2005). Cleavage pattern and emerging asymmetry of the mouse embryo. Nat. Rev. Mol. Cell Biol. 6, 919–928. https://doi.org/10. 1038/nrm1782.
- Olivier, N., Luengo-Oroz, M.A., Duloquin, L., Faure, E., Savy, T., Veilleux, I., Solinas, X., Débarre, D., Bourgine, P., Santos, A., et al. (2010). Cell lineage reconstruction of early zebrafish embryos using label-free nonlinear microscopy. Science 329, 967–971. https://doi.org/10.1126/science. 1189428.
- Gilbert, S.F. (2010). Developmental Biology, Ninth Edition (Sinauer Associates).
- Sallé, J., Xie, J., Ershov, D., Lacassin, M., Dmitrieff, S., and Minc, N. (2019).
   Asymmetric division through a reduction of microtubule centering forces.
   J. Cell Biol. 218, 771–782. https://doi.org/10.1083/jcb.201807102.
- Tanimoto, H., Sallé, J., Dodin, L., and Minc, N. (2018). Physical Forces Determining the Persistency and Centering Precision of Microtubule Asters. Nat. Phys. 14, 848–854. https://doi.org/10.1038/s41567-018-0154-4
- Xie, J., Najafi, J., Le Borgne, R., Verbavatz, J.-M., Durieu, C., Sallé, J., and Minc, N. (2022). Contribution of cytoplasm viscoelastic properties to mitotic spindle positioning. Proc. Natl. Acad. Sci. USA 119, e2115593119.
- Hiramoto, Y. (1969). Mechanical properties of the protoplasm of the sea urchin egg. I. Unfertilized egg. Exp. Cell Res. 56, 201–208. https://doi. org/10.1016/0014-4827(69)90003-2.



- Najafi, J., Dmitrieff, S., and Minc, N. (2023). Size- and position-dependent cytoplasm viscoelasticity through hydrodynamic interactions with the cell surface. Proc. Natl. Acad. Sci. USA 120, e2216839120. https://doi.org/10. 1073/pnas.2216839120.
- Garzon-Coral, C., Fantana, H.A., and Howard, J. (2016). A force-generating machinery maintains the spindle at the cell center during mitosis. Science 352, 1124–1127. https://doi.org/10.1126/science.aad9745.
- Howard, J., and Garzon-Coral, C. (2017). Physical Limits on the Precision of Mitotic Spindle Positioning by Microtubule Pushing forces: Mechanics of mitotic spindle positioning. BioEssays 39, bies.201700122. https:// doi.org/10.1002/bies.201700122.
- Bai, L., and Mitchison, T.J. (2022). Spring-like behavior of cytoplasm holds the mitotic spindle in place. Proc. Natl. Acad. Sci. USA 119, e2203036119.
- Wang, H., Li, Y., Yang, J., Duan, X., Kalab, P., Sun, S.X., and Li, R. (2020). Symmetry breaking in hydrodynamic forces drives meiotic spindle rotation in mammalian oocytes. Sci. Adv. 6, eaaz5004. https://doi.org/10.1126/ sciadv.aaz5004.
- Lacroix, B., Letort, G., Pitayu, L., Sallé, J., Stefanutti, M., Maton, G., Ladouceur, A.M., Canman, J.C., Maddox, P.S., Maddox, A.S., et al. (2018). Microtubule Dynamics Scale with Cell Size to Set Spindle Length and Assembly Timing. Dev. Cell 45, 496–511.e6.
- Anjur-Dietrich, M.I., Hererra, V.G., Farhadifar, R., Wu, H., Merta, H., Bahmanyar, S., Shelley, M.J., and Needleman, D.J. (2023). Clustering of cortical dynein regulates the mechanics of spindle orientation in human mitotic cells. Preprint at bioRxiv. https://doi.org/10.1101/2023.09.11. 557210.
- Deneke, V.E., Puliafito, A., Krueger, D., Narla, A.V., De Simone, A., Primo, L., Vergassola, M., De Renzis, S., and Di Talia, S. (2019). Self-Organized Nuclear Positioning Synchronizes the Cell Cycle in Drosophila Embryos. Cell 177, 925–941.e17. https://doi.org/10.1016/j.cell.2019.03.007.
- Yi, K., Unruh, J.R., Deng, M., Slaughter, B.D., Rubinstein, B., and Li, R. (2011). Dynamic maintenance of asymmetric meiotic spindle position through Arp2/3-complex-driven cytoplasmic streaming in mouse oocytes. Nat. Cell Biol. 13, 1252–1258. https://doi.org/10.1038/ncb2320.
- Middelkoop, T.C., Neipel, J., Cornell, C.E., Naumann, R., Pimpale, L.G., Jülicher, F., and Grill, S.W. (2024). A cytokinetic ring-driven cell rotation achieves Hertwig's rule in early development. Proc. Natl. Acad. Sci. USA 121, e2318838121. https://doi.org/10.1073/pnas.2318838121.

- Happel, J., and Brenner, H. (2012). Low Reynolds Number Hydrodynamics: with Special Applications to Particulate Media (Springer Science & Business Media).
- Nazockdast, E., Rahimian, A., Zorin, D., and Shelley, M. (2017). A fast platform for simulating semi-flexible fiber suspensions applied to cell mechanics. J. Comp. Phys. 329, 173–209.
- Shamipour, S., Kardos, R., Xue, S.-L., Hof, B., Hannezo, E., and Heisenberg, C.-P. (2019). Bulk Actin Dynamics Drive Phase Segregation in Zebrafish Oocytes. Cell 177, 1463–1479.e18. https://doi.org/10.1016/ j.cell.2019.04.030.
- Niwayama, R., Shinohara, K., and Kimura, A. (2011). Hydrodynamic property of the cytoplasm is sufficient to mediate cytoplasmic streaming in the Caenorhabiditis elegans embryo. Proc. Natl. Acad. Sci. USA 108, 11900–11905. https://doi.org/10.1073/pnas.1101853108.
- Goldstein, R.E., Tuval, I., and van de Meent, J.-W. (2008). Microfluidics of cytoplasmic streaming and its implications for intracellular transport. Proc. Natl. Acad. Sci. USA 105, 3663–3667. https://doi.org/10.1073/pnas. 0707223105.
- He, B., Doubrovinski, K., Polyakov, O., and Wieschaus, E. (2014). Apical constriction drives tissue-scale hydrodynamic flow to mediate cell elongation. Nature 508, 392–396. https://doi.org/10.1038/nature13070.
- Foe, V.E., and von Dassow, G. (2008). Stable and dynamic microtubules coordinately shape the myosin activation zone during cytokinetic furrow formation. J. Cell Biol. 183, 457–470. https://doi.org/10.1083/jcb. 200807128.
- Ettensohn, C.A., Wessel, G.M., and Wray, G. (2004). Development of Sea Urchins, Ascidians, and Other Invertebrate Deuterostomes: Experimental Approaches, [1st Edition], 74 (Elsevier). https://shop.elsevier.com/books/ development-of-sea-urchins-ascidians-and-other-invertebrate-deuterostomesexperimental-approaches/ettensohn/978-0-12-480278-0.
- Chenevert, J., Robert, M.L.V., Sallé, J., Cacchia, S., Lorca, T., Castro, A., McDougall, A., Minc, N., Castagnetti, S., Dumont, J., et al. (2024). Measuring Mitotic Spindle and Microtubule Dynamics in Marine Embryos and Non-model Organisms. Methods Mol. Biol. 2740, 187–210.
- Thielicke, W., and Stamhuis, E.J. (2014). PIVIab Towards User-friendly, Affordable and Accurate Digital Particle Image Velocimetry in MATLAB.
   J. Open Res. Software 2, e30. https://openresearchsoftware.metajnl.com/articles/10.5334/jors.bl.





#### **STAR**\*METHODS

#### **KEY RESOURCES TABLE**

REAGENT or RESOURCE	SOURCE	IDENTIFIER
Antibodies		
Mouse anti-α-tubulin DM1A	Sigma-Aldrich	T9026; PRID:AB_477593
anti-mouse Dylight 488	Thermo Fisher Scientific	35502
anti-rabbit Dylight 650	Thermo Fisher Scientific	84546
Bacterial and virus strains		
BL21 (DE3)-RIL Competent cells	Agilent	230245
Chemicals, peptides, and recombinant protein	s	
DMSO	Euromedex	UD8050
Triton X-100	Sigma-Aldrich	T8787
HEPES	Sigma-Aldrich	H3375
EGTA	Sigma-Aldrich	E3889
Triton X-100	Sigma-Aldrich	T8787
Formaldehyde 16% (w/v), methanol free	Thermo Fisher Scientific	28908
NaBH <sub>4</sub>	Sigma-Aldrich	D282
Glutaraldehyde Grade I, 25%	Sigma-Aldrich	G5882
Glycerol	Sigma-Aldrich	G5516
N-Propyl gallate (HPLC)	Sigma-Aldrich	02370
Protamine sulfate	Sigma-Aldrich	P4020
Tween® 20	Sigma-Aldrich	P1379
ATTO-565-biotin	Sigma-Aldrich	92637
Hoechst	Sigma-Aldrich	33342
Rhodamine Phalloidin	Invitrogen	R415
Others		
800 nm streptavidin magnetic beads	NanoLink; Solulink	M-1002-020
1 μm streptavidin magnetic beads	Thermo Fisher Scientific	65001
Artificial seawater (Reef Crystal)	Instant Ocean	RC15-10
Sigmacote	Sigma-Aldrich	SL2
SU8	Microchem	SU8-2050
Software and algorithms		
Finite element simulation software	COMSOL	COMSOL multiphysics
Image analysis software	FIJI	FIJI
Statistical analysis and curve fitting software	MATHWORKS	MATLAB

#### **EXPERIMENTAL MODEL AND SUBJECT DETAILS**

#### Sea urchin gametes

Purple sea urchins (*Paracentrotus lividus*) were obtained from the Roscoff Marine station (France) and maintained at 16°C in artificial sea water (ASW; Reef Crystals, Instant Ocean). Gametes were collected by intracoelomic injection of 0.5 M KCl. Sperm was collected undiluted, kept at 4°C and used within one week. Eggs were rinsed twice with ASW, kept at 16°C, and used on the day of collection.

## **Current Biology** Report



Unfertilized eggs were transferred on protamine-coated glass-bottom dishes (MatTek Corporation) after removing the jelly coat through an 80-μm Nitex mesh (Genesee Scientific), injected and fertilized under the microscope.

#### **METHOD DETAILS**

#### **Immunostaining**

Immunostaining was performed using procedures described previously. 40 First, to remove the fertilization envelope and facilitate Antibody penetration, eggs are fertilized in a fresh solution of p-aminobenzoic acid (PABA) in ASW for 3 minutes, washed 3 times in ASW, and incubated at 16°C until the desired stage. Then, samples were fixed for 70 min in 100 mM Hepes, pH 6.9, 50 mM EGTA, 10 mM MgSO4, 2% formaldehyde, 0.2% glutaraldehyde, 0.2% Triton X-100, and 400 mM glucose. To reduce autofluorescence, eggs were then rinsed 3 times in PBS and placed in 0.1% NaBH4 in PBS freshly prepared, for 30 min. Eggs were rinsed with PBS and PBT (PBS + 0.1% TritonX) and blocked in PBT supplemented with 5% goat serum and 0.1% bovine serum albumin (BSA) for 30 min. Samples were rinsed with PBT before adding primary antibodies. For MT staining, cells were incubated for 48 h at 4°C with either a mouse anti-α-tubulin (DM1A; Sigma-Aldrich) primary antibody at 1:5000 in PBT, or a YL1/2 rat anti-tubulin (Abcam) primary antibody at 1:1000 in PBT, or a rabbit anti-KDEL (Invitrogen) primary antibody at 1:2,000 to stain the ER, rinsed 3 times in PBT and incubated for 4 h at room temperature with anti-mouse, anti-rat or anti-rabbbit secondary antibody coupled to Dylight fluorophores (Thermo Fisher Scientific), or a secondary alpaca nanobody anti-mouse 488 SMS1AF488-1-100 (Thermo Fisher Scientific) at 1:1000 in PBT. DNA was stained with 10  $\mu$ g.ml<sup>-1</sup> Hoechst 33342 (Sigma-Aldrich) in PBT during the same step as for the secondary antibody. For actin staining, samples were incubated for 1h in a solution of Rhodamine Phalloidin at 4U/ml in PBT. Eggs were washed three times in PBT then twice in PBS, transferred in 50% glycerol in PBS, and finally transferred into mounting medium (90% glycerol and 0.5% N-propyl gallate PBS). For staining from the 1-cell stage to the 16-cell stage, samples were fixed at different times after fertilization, with a time interval of around one hour. Fixation times for metaphase cells at different stages were performed at 45-55 min post-fertilization for the 1-cell stage, 1h45-1h55min for the 2-cell stage, 2h45-2h55min for the 4-cell stage, 3h45-3h55min for the 8-cell stage, and 4h45-4h55min for the 16-cell stage.

#### Manipulating cell shape with CaFSW

To manipulate cell shape at the 2-cell stage from a hemisphere to a sphere, magnetic bead-injected eggs were first fertilized and incubated in para-aminobenzoic acid (PABA) for 2 min to soften the fertilization envelope, and PABA was then washed out by rinsing in ASW. The softened fertilization envelop was cut to open a hole using a glass capillary. After the first cell division, interphase cells were incubated in Hyaline Extract Medium (HEM) for 2 minutes, then rinsed with calcium free sea water (CaFSW) to disassemble cell-cell junctions (protocol adapted from Ettensohn et al. 41). Cells became round and were able to separate from their sister cells after pushing a cell out of the fertilization envelope through the opening. The remaining cell inside the fertilization envelope containing magnetic beads was imaged and its spindle was moved with magnetic tweezers at 2-cell metaphase. After CaFSW treatment, cells formed normal spindles and underwent normal cytokinesis with spindle length and metaphase duration similar to controls (Figure S2).

#### **Fabrication of microchambers**

Resin-made microchambers were produced using standard photolithography on a coverglass. A large glass coverslip (50 \* 75 mm) was first cleaned with acetone, isopropanol and DI water, and then dried with compressed air, and heated at 95°C on a hotplate for 2 minutes to evaporate any remaining chemicals. After cleaning, a first layer of Omnicoat (MicroChem) was deposited with a spin-coater at 4000 rpm, and then dried for 2' at 95°C. A layer of SU8-2050 resin (MicroChem) was then deposited with a spin-coater at 2500 rpm and baked for 3' at 65°C and 9' at 95°C. The coverslip was then exposed to UV light for 14 seconds to polymerize the resin through a photomask with different U-shape designs. The coverslip was baked again, and developed in SU8 developer solution for 5 minutes and rinsed extensively with isopropanol. Finally, the coverslip was baked at 120°C for 10 minutes and allowed to cool gradually to room temperature. A mini-wall made of Bondic UV glue was assembled around the coverslip to form a reservoir allowing to place liquid onto the chambers. Finally, the chambers were rinsed in PBS for more than 48 h to remove any soluble chemicals from the microfabrication process.

#### Manipulating cell shape with microchambers

To manipulate the shape of zygotes, from a sphere to a rectangle, the resin U-chambers were first plasma-cleaned and coated with 1% protamine. Using a microforge (Narishige MF2), a non-siliconized glass needle was cut and melted to obtain a smooth tip with an opening of  $\sim$ 20-30  $\mu$ m, then bent at 30° and installed on a secondary hydraulic micromanipulator (Narishige NAI-30). The needle was connected to a hydraulic pressure controller (Eppendorf, CellTram) and used as holding pipette. Sea urchin eggs were placed on the chamber using the holding pipette, and gently pushed to fill the chamber shape. The eggs were pushed inside the chamber and injected with magnetic beads. After fertilization, metaphase zygotes with beads attached to one spindle pole were selected for force application using magnetic tweezers. Cells inside the chambers formed normal spindles and underwent normal cytokinesis but with a slightly longer metaphase duration than controls (Figure S3).





#### **Magnetic force application**

Magnetic tweezers were implemented as described previously.  $^{20-22}$  The magnet probe used for force applications *in vivo* was built from three rod-shaped strong neodymium magnets (diameter 4 mm; height 10 mm; S-04-10-AN; Supermagnet) prolonged by a sharpened steel piece with a tip radius of  $\sim$ 50  $\mu$ m to create a magnetic gradient. The surface of the steel tip was electro-coated with gold to prevent oxidation. The probe was controlled with a micromanipulator (Injectman 4, Eppendorf), and mounted on an inverted epifluorescence microscope.

Super-paramagnetic particles (diameter 800nm; NanoLink; Solulink) with spontaneous MT minus end–directed motion were used to apply magnetic forces on the spindles for early blastomeres or cells shaped with CaFSW or microchambers.  $^{20-22}$  To prepare beads for injection, a solution of 10  $\mu$ l of undiluted streptavidin-beads was first washed in 100  $\mu$ L of washing solution (1 M NaCl with 1% Tween-20), and sonicated for 5 min. The beads were then rinsed in 100  $\mu$ l PBS, incubated 15 min in 100  $\mu$ l 2  $\mu$ g/ml Atto565-biotin (Sigma-Aldrich), rinsed again in 100  $\mu$ l PBS, and finally re-suspended in 20  $\mu$ l PBS and kept at 4°C until use. Unfertilized eggs were placed on a protamine-coated glass bottom dish or inside a protamine-coated microchamber. The bead solution was injected using a micro-injection system (FemtoJet 4, Eppendorf) and a micro-manipulator (Injectman 4, Eppendorf). Injection needles were prepared from siliconized (Sigmacote) borosilicate glass capillaries (TW100-4) of 1 mm in diameter. Glass capillaries were pulled using a needle puller (P-1000, Sutter Instrument) and ground with a 40° angle on a diamond micro-grinder (EG-40, Narishige) to obtain a 10  $\mu$ m aperture. Injection needles were back-loaded with 2  $\mu$ l of bead solution before each experiment, and were not re-used. After fertilization, beads were spontaneously transported along MTs and formed a large aggregate at the center of the aster. This aggregate stayed stably at the centrosome and occasionally split at centrosome duplication. Thus, at metaphase, beads sometimes ended up on one or the two spindle poles. The targeting of beads towards the centrosomes presumably occurred in a dynein- and microtubule-dependent manner.  $^{22}$ 

To image spindle displacement under force, unfertilized eggs stuck on protamine-coated glass dishes or inside a protamine-coated U chamber were incubated in  $10 \mu g/ml$  Hoechst (Sigma-Aldrich) before injection and fertilization. At metaphase, chromosomes marked with Hoechst, lined up along the metaphase plate, and the spindle was easily visible as a dumbbell-shaped smooth region in DIC (Differential Interference Contrast), presumably because of its association with the ER. These DIC images allowed to select spindles that were planar and to define the long and short-axis directions for force applications. The magnet was then rapidly moved close to the eggs and held at a fixed position along the spindle axis (see Video S2). The end of metaphase was captured as the first time-point when chromosomes separated. Importantly, pulling experiments were limited to a small enough displacement, calculated from the size and distance of MTs to the cortex at each developmental stage, that ensured that mitotic asters did not come into contact with the cortex.

#### **Imaging**

Time-lapses of spindles and  $1\mu m$  magnetic beads moving under magnetic force were recorded on two inverted microscope set-ups equipped with a micromanipulator for magnetic tweezers, at a stabilized room temperature (18–20°C). The first set-up was an inverted epifluorescence microscope (TI-Eclipse, Nikon) combined with a complementary metal–oxide–semiconductor (CMOS) camera (Hamamatsu), using a 20X dry objective (Apo, NA 0.75, Nikon) and a 1.5X magnifier, yielding a pixel size of 0.216  $\mu m$ . The second one was a Leica DMI6000 B microscope equipped with an A-Plan 40x/0.65 PH2 objective yielding a pixel size of 0.229  $\mu m$ , equipped with an ORCA-Flash4.0LT Hamamatsu camera. Both microscopes were operated with Micro-Manager (Open Imaging).

Imaging of immunostained cells to visualize MTs or F-actin was performed on a confocal microscope (Zeiss, LSM980) coupled to an Airyscan 2 module in confocal mode with a 63X water immersion objective (NA, 1.4; C-Apo; Zeiss).

Imaging of dynamic microtubules for quantification of growth rate was achieved by injecting ATTO 565-tubulin at 2 mg/ml before fertilizing embryos. Images were acquired on a single channel (561 nm excitation) every 1 sec with a single z-plan.<sup>29,42</sup>

#### 3D simulations

The spindle pulling experiments at various cell division stages were modeled using the finite element software COMSOL as described in previous studies. <sup>24,28</sup> The viscoelastic parameters of the cytoplasm  $\gamma_1$ ,  $\gamma_2$ , and  $\kappa$  at different cell stages were measured by fitting a Jeffreys' model to the averaged creep curve of magnetic beads with a radius r=0.5 μm, moved in the zygote cytoplasm in mitosis. These values were converted to the equivalent values in the Oldroyd-B model and inserted into the simulations as  $\eta_1$ ,  $\eta_2$ , and  $\tau_2$ , where  $\eta_{1,2}$  is the viscosity experienced by the bead and obtained using Stokes' law  $\gamma = 6\pi\eta r$ , and  $\tau_2 = \gamma_2/\kappa$  represents the characteristic time scale of the fluid. Viscosities were corrected using the coefficient for two parallel confining planes before being inserted in the model. Two sets of simulations were performed to investigate the effect of cell size and shape, at different stages on the viscous drag and restoring stiffness. In the first set of simulations, cell shape was assumed to be round, and only the cell and spindle size were modified. In a second set, cell shapes, sizes and spindles sizes were changed according to experiments (Figures 2 and S1). The shape of the cell boundary in the first division stage was a sphere with the radius R. To simplify cell shape modifications during cell division, we assumed that in the second and fourth division stages, the cell shapes were equivalent to half and one-fourth of a sphere with the same radius as the first cell stage. To simulate eggs in the microchambers, the width and length of the rectangular cube confinements were inserted from the cell shape in the experiments and the height was calculated using the volume of the spherical cells. Moreover, a set of simulations was done to inspect the consequence of the cross-section on the viscoelastic properties in the rectangular chambers (Figures S3M and S3N). In this series, the volume of the chambers was the same as a spherical cell at the first division stage. The length of the chambers was constant and only the cross-section was changed from a square to a long



rectangle. As spindles are enclosed in a dense ER network, the spindle was considered as a rigid elastic (prolate) ellipsoid with long semi-axis a and short semi-axis b which were measured from the outer ellipsoidal contour of spindles (Figure S1K). The spindle was placed in the origin of the coordinate system in the geometrical center of the cells. The spindle dimensions were constant at each cell division stage in the simulations but were slightly reduced from the first to the fourth stage, as in experiments. The cytoplasm was interacting with the pulled spindle by including viscoelastic flow and solid mechanics modules in COMSOL through stress at the boundaries. The viscoelastic flow module solves the Navier-Stokes and continuity equations:

$$\rho \frac{\partial \boldsymbol{u}}{\partial t} + \rho(\boldsymbol{u}.\nabla)\boldsymbol{u} = \nabla \cdot [-\rho \boldsymbol{I} + \boldsymbol{K} + \boldsymbol{T}_{e}] + \boldsymbol{F}$$

$$\rho \nabla . \boldsymbol{u} = 0$$

$$K = \mu_s S$$

$$S = \left(\nabla \boldsymbol{u} + (\nabla \boldsymbol{u})^T\right)$$

$$\lambda_{e_m} \frac{\Delta \boldsymbol{T}_e}{\Delta t} + \boldsymbol{T}_e = 2\mu_e \mathbf{S}$$

where  $\rho$ ,  $\mathbf{u}$ , and  $\mathbf{p}$  are the density, velocity, and pressure of the fluid, respectively.  $\mathbf{I}$  is an identity matrix,  $\mathbf{K}$  represents the viscous stress tensor due to the viscosity of the solvent fluid, and  $\mathbf{T}_e$  indicates the elastic stress.  $\mathbf{F}$  is the body force acting on the fluid.  $\mu_s$  is the solvent viscosity,  $\lambda_e$  and  $\mu_e$  /  $\lambda_e$  are the viscoelastic time scale and the elastic modulus respectively, and  $\mathbf{S}$  is the strain rate tensor. Both  $\mu_s$  and  $\mu_e$  contribute to  $\eta_1$  and  $\eta_2$ . The spindle was described as a linear solid elastic material, with the stress at the boundary equal to the stress of the visco-elastic fluid at the boundary by continuity. We found that the exact elastic properties of the solid did not play a role in the fluid mechanics within the experimental stress range. The governing equations for the solid mechanics module for the time-dependent study describes the motion of solid materials under deformation, stress, and external forces:

$$\rho \frac{\partial^2 \textbf{u2}}{\partial t^2} \ = \ \nabla. (FS)^T + \textbf{F}_v$$

$$\mathbf{F} = \mathbf{I} + \nabla \mathbf{u} \mathbf{2}$$

$$S = S_{add}JF_{inel}^{-1}(C:\epsilon_{el})F_{inel}^{-T}$$

where  $\rho$  and  $\mathbf{u2}$  are the density and displacement vector fields within the solid material.  $\nabla$  .( $\mathbf{FS}$ )<sup>T</sup> describes the distribution of internal stresses within the material, where  $\mathbf{F}$  is the deformation gradient tensor indicating how the solid material is stretched, compressed, or deformed, and is given by the second equation.  $\mathbf{S}$  is the second Piola-Kirchhoff stress tensor, representing stress in the material in its undeformed configuration and describing internal forces and stresses that arise from the deformation of the solid body.  $\mathbf{J}$ ,  $\mathbf{F}_{\text{inel}}$ , and  $\mathbf{\epsilon}_{\text{el}}$  are determinant of the deformation gradient, inelastic deformation gradient, and elastic strain, respectively.  $\mathbf{C}$  is the material stiffness matrix which depends on Young's modulus and Poisson's ratio through the material parameters of modeled spindle. And  $\mathbf{Fv}$  is the external force applied to the spindle. All geometrical parameters were inserted using measured values from experiments. A Heaviside step function was used to apply a constant force as a boundary load on half of the ellipsoid. The force direction was along the long axis of the ellipsoid for the translational displacement, and was perpendicular to the long axis at the initial time for the orthogonal displacement. The amplitude of loads in the time-dependent model was equal to the average magnetic forces in the experiments applied for 150 seconds and then released. The boundary conditions were no-slip and simulations were performed using a normal mesh size.

The viscoelastic parameters of simulation results were derived from the creep curve, as experimental curves, and fits of the Jeffreys model were performed by optimization method with a custom-written MATLAB script. Only the first frame of the pulling phase was used for the measurement of the vortex sizes in the simulations. The input parameters of the simulations are summarized in Table S1.





#### **QUANTIFICATION AND STATISTICAL ANALYSIS**

#### **Magnetic force calibration**

Magnetic forces were calibrated *in vitro* following procedures described previously.  $^{20-22}$  The magnetic force field created by each magnet tip used was first characterized by pulling 2.8  $\mu$ m mono-dispersed magnetic beads (M-280 Dynabeads) in a viscous test fluid (80% glycerol, viscosity 8.0×10–2 Pa sec at 22°C) along the principal axis of the magnet tip. Small motion of the fluid was subtracted by tracking 4  $\mu$ m non-magnetic fluorescent tracers in the same solution. The speed of a magnetic bead V was computed as a function of the distance to the magnet, representing the decay function of the magnetic force, and fitted using a double exponential function.

To compute the dependence of the force on aggregate size, bead aggregates from the same beads as those used *in vivo* in sizes ranging from 2 to 8  $\mu$ m, similar to that observed in cells, were pulled in the same fluid as above. The speed  $V_a$  was measured and translated into a force using Stokes' law  $F=6\pi\eta RV_a$ , where  $\eta$  was the viscosity of the test fluid, R the aggregate effective radius defined using the longest length  $L_1$  and the length perpendicular to the longest axis,  $L_2$ , as  $R=\frac{1}{2}\sqrt{L_1L_2}$ . The force–size relationship at a fixed distance from the magnet was well represented and fitted by a cubic function. These speed–distance and force–size relationships were combined to compute the magnetic forces applied to spindles inside cells as a function of time, from the size of aggregates at spindle poles and their distance to magnet tips. Importantly, uncertainties in fitting parameters and bead aggregate size estimates, led to errors in force estimation that we estimated to be around 10-50%. These errors probably contribute to an important fraction of the noise in the estimated viscoelastic parameters associated to spindle force application throughout the manuscript.

In each live cell experiment, the dimensions of the bead aggregates attached to spindle poles were measured at three different positions in fluorescence and averaged; and the distance to the magnet tip was computed at each time frame during spindle pulls; allowing to compute net forces applied to spindles as a function of time. In general, forces did not vary more than 5-10% during each individual pull. The net magnetic forces applied to spindles in cells, in all experiments presented in this work ranged from  $\sim$ 100 up to 1000 pN. The mean force applied to spindles was 371.7 pN +/- 168pN (+/- S.D.) at the 1-cell stage; 384.8 pN +/- 266.8 pN at the 2-cell stage and 340.3 pN +/- 173pN at the 4-cell stage.

#### **Analysis of spindle position**

Spindle displacement time-lapses were rotated to align the initial spindle axis to the horizontal X-axis. Magnet tip position was recorded in DIC and the position of bead aggregates was tracked from their fluorescence signal. Spindle position was processed manually in Fiji by tracking the centers of two smooth disks, which correspond to ER-enriched spindle poles in the DIC channel. This allowed to compute spindle length, center as well as angles with the magnetic force axis. Spindle displacements and magnetic forces were then projected along the horizontal X-axis. Chromosome plate position was also tracked but we often noticed some small delay in the motion of chromosomes as compared to that of spindle poles, presumably caused by some time-scales associated with internal elastic structures that hold chromosomes. In some experiments in which cells were treated with CaFSW, the cell moved during the pull, so the spindle position was corrected according to the displacement of the cell.

#### Measuring MT length, dynamics and distance to the cortex

Airyscan confocal images stained for MTs and F-actin from the 1-cell to the 16-cell stages were projected onto a mid-section 2  $\mu$ m thick, and planar spindles were selected. The distance between MT + TIPs to the actin cortex were measured, by tracing lines along each MTs to the first border of the F-actin signal using Fiji, and identifying points at which signal intensity drops or increases in both MT and actin channels. Normalization of the distance between MTs and cortex was computed using the cell length along the spindle axis. Astral MT length was also computed using line traces in Fiji. Astral MT growth rate was computed using kymographs that were traced from time-lapse sequences in Fiji. Polymerization rates, were extracted from these kymographs by manual tracking and semi-automated parameter extraction using homemade macros in Fiji and Excel (Microsoft).  $^{29,42}$ 

#### Viscoelastic parameter calculation

Displacements of spindles were fitted with a Jeffreys' model using a custom code written in MATLAB (Mathworks) to compute viscoelastic parameters. For the rising phase, the spindle position was fitted using:

$$\frac{d(t)}{F(t)} = \frac{1}{\kappa} \left[ 1 - e^{-\frac{t}{\tau^1}} \right] + \frac{t}{\kappa \tau^2},$$

where d is the displacement along the X-axis, and F is the magnetic force. These fits allowed to compute the restoring stiffness,  $\kappa$ , and the viscoelastic time-scales,  $\tau_1$  and  $\tau_2$  corresponding to the Jeffreys' viscoelastic timescales, allowing to compute viscous drags on spindles as  $\gamma = \kappa \tau$ .

Spindle relaxation dynamics was fitted using:

$$\frac{d(t)}{d(0)} = (1-a)e^{-\frac{t}{\tau t}} + a$$

where t = 0 corresponds to the time of the end of force application, to compute the relaxation offset a and the relaxation time-scale  $\tau_r$ .

## **Current Biology** Report



Fit of the data were obtained for each single force experiment, using Nonlinear least squares method in MATLAB curve fitting. Various combinations of starting points of fit parameters were tried and chosen in a way that maximum R-squared values and tighter confidence interval were achieved. Curves were also visually inspected to ensure that they passed through more points and were not biased with respect to the data points.

#### PIV analysis and shear measurement

The recorded image sequences of spindle pulling in DIC were analyzed using the particle image velocimetry PIVlab tool in MATLAB (Mathwork). <sup>43</sup> The exterior of the egg was masked to be excluded from the analysis. Contrast limited adaptive histogram equalization (CLAHE) and two-dimensional Wiener filter with accordingly windows of 20 and 3 pixels widths were applied on the images in the preprocessing steps for denoising. Image sequences were analyzed in the Fourier space by three interrogation windows with 64, 32, and 16 pixels widths and 50% overlapped area. The spline method was used for the window deformation, and subpixel resolution was obtained by two-dimensional Gaussian fits. The distribution of the velocity components of all vectors for each set was visually inspected and restricted to remove the outliers in the post-processing stage. Moreover, two other filters based on the standard deviation and local median of velocity vectors were applied to validate the vector fields. The output vector fields after smoothing were used for the analysis. The vector fields were temporally averaged over the first five frames of the pulling phase before heat map plotting and vortex analysis.

To estimate vortex size, the component of the vector field along the pulling axis x was spatially averaged over half of the egg close to the magnet after the temporal average of the velocity field. Two Gaussian functions were fitted to the side peaks of the velocity profile. These peaks started from the middle of the vortices around the spindle and extended up to the cell surface where the flow was affected by the boundary confinement. The size of vortices was calculated as the width of the Gaussian function and averaged over both sides for each sample (Figure S3H).

#### Statistical analysis

All experiments presented in this manuscript were repeated at least twice and quantified in a number of cells or events detailed in each figure legend. Statistical and correlation analyses were carried out using Prism 6 (GraphPad Software, La Jolla, CA), Matlab or excel. Statistically significant differences and tests used depended on whether experiments were paired or not and are reported in figure legends.